OCEANOGRAPHY

# The Mediterranean Overflow in the Gulf of Cadiz: A rugged journey

Ricardo F. Sánchez-Leal,[1]* María Jesús Bellanco,[1] Luis Miguel Fernández-Salas,[1] Jesús García-Lafuente,[2] Marc Gasser-Rubinat,[3] César González-Pola,[4] Francisco J. Hernández-Molina,[5] Josep L. Pelegrí,[3] Alvaro Peliz,[6] Paulo Relvas,[7] David Roque,[8] Manuel Ruiz-Villarreal,[9] Simone Sammartino,[2] José Carlos Sánchez-Garrido[2]



**The pathways and transformations of dense water overflows, which depend on small-scale interactions between flow dynamics and erosional-depositional processes, are a central piece in the ocean's large-scale circulation. A novel, high-resolution current and hydrographic data set highlights the intricate pathway travelled by the saline Mediterranean Overflow as it enters the Atlantic. Interaction with the topography constraints its spreading. Over the initial 200 km west of the Gibraltar gateway, distinct channels separate the initial gravity current into several plunging branches depth-sorted by density. Shallow branches follow the upper slope and eventually detach as buoyant plumes. Deeper branches occupy mid slope channels and coalesce upon reaching a diapiric ridge. A still deeper branch, guided by a lower channel wall marked by transverse furrows, experiences small-scale overflows which travel downslope to settle at mid-depths. The Mediterranean salt flux into the Atlantic has implications for the buoyancy balance in the North Atlantic. Observations on how this flux enters at different depth levels are key to accurately measuring and understanding the role of Mediterranean Outflow in future climate scenarios.**

## INTRODUCTION

Tectonic activity at the end of the Miocene (*1*) along with later Zanclean flooding [5.33 million years ago (Ma); (*2*)] and coeval regressive erosion (*3*) led to the formation of the shallow Strait of Gibraltar, an oceanographic gateway connecting Mediterranean and Mid-Atlantic water masses. Negative freshwater fluxes and winter cooling in the Mediterranean generate sharp density gradients that drive an inverse estuarine circulation that transports a bottom outflow [~1 sverdrup (Sv) ($10^6$ $m^3/s$)] of dense ($\sigma_\Theta$ = 29.07 kg $m^{-3}$), cold (12.9°C), and saline (38.45) Mediterranan Outflow Water (MOW) and a surface inflow (~1.05 Sv) of warmer (16.6° to 22.6°C), less saline (36.5) Atlantic Inflow (AI) Water (as used in the literature, we refer to the underflow out of the Mediterranean as the Outflow). This flow across the Spartel Sill (last threshold at the western end of the Strait; see fig. S1) is separated by a sharp interface at about 200-m depth (*4*, *5*). The dense MOW then cascades into the Gulf of Cadiz (GoC). Since the late Neogene, this flow has developed an impressive channel system, first as a weak undercurrent (5.2 to 3.2 Ma), then as a fully developed gravity overflow and erosive bottom current [2 Ma to present; (*6*)]. This site of current-topography interaction represents an excellent example of tectonic-climatic interactions, where bathymetry [strait sills (*7*) and diapiric ridges (*8*)] modulates overflow behavior (*9*).

The MOW pathway into the Atlantic first runs through a linear, 40-km long channel interrupted by irregular bathymetric features. It is then guided into a concavity consisting of two large erosive channels that conduct the flow in a clockwise (to the right) direction (*10*, *11*). West of 7.0°W (some 150 km past Spartel), the MOW reaches geostrophic balance (*5*) as a double-cored, neutrally buoyant saline plume that separates from the slope at depths of 800 to 1200 m and with flow rates of up to 2.5 Sv (*12*). This final product spreading across the Atlantic is commonly referred to as the Mediterranean, Mediterranean Overflow, or Outflow Water, a distinct water mass with the source at the GoC composed of one-third pure Mediterranean water and two-thirds Eastern North Atlantic Central Water (ENACW). Counting coherent lenses [meddies (*13*)] and double diffusion (*14*), the relative MOW contribution to the negative freshwater balance in the subtropics reaches 30% (*15*). This contribution is partly responsible for (NADW) relatively high North Atlantic salinities (*16*), which facilitate buoyancy loss at high latitudes and precondition the formation of North Atlantic Deep Water (NADW) Circulation (*9*). The MOW supplement boosts Atlantic Meridional Overturning Circulation (AMOC) (*17*) and stabilizes North Atlantic climate within the range of variation observed over the past 2 Ma (*9*). The MOW also stimulates the Azores Current system (*18*) and the onset of the GoC Current at local scales (*19*). To study the role of Mediterranean salinity in North Atlantic climate dynamics, oceanographic measurement strategies and regional climate modeling can benefit from a more detailed understanding of the Mediterranean Outflow.

Here, we present a novel, high-resolution view of near-bottom conductivity-temperature-depth (CTD) and current velocity observations acquired over the last 50 years (see figs. S1 and S2). The data offer a detailed picture of a complex transition from a single-point, dense overflow at Spartel to a multicored buoyant saline plume in the western GoC. Bathymetric features strongly influence the initial conditions of the MOW and thus determine fundamental spatial and hydrodynamic constraints on its ultimate integration with other Atlantic water masses. The results presented here complement and quantify recent high-resolution mapping efforts of the GoC seafloor west of Gibraltar (*10*, *20*). Our description of this oceanographic transition demonstrates the interplay

[1]Spanish Institute of Oceanography, Cadiz Oceanographic Center, Muelle de Levante s/n, Puerto Pesquero, Cádiz E11006, Spain. [2]University of Malaga Physical Oceanography Group (GOFIMA), ETSI Telecomunicación, Campus de Teatinos s/n, Málaga E29071, Spain. [3]Department of Physical and Technological Oceanography, Institute of Marine Sciences (CSIC), Passeig Marítim de la Barceloneta 37-49, Barcelona E08003, Spain. [4]Spanish Institute of Oceanography, Gijón Oceanographic Center, Avenida Príncipe de Asturias 70 bis, Gijón E33212, Spain. [5]Department of Earth Sciences, Royal Holloway, University of London, Egham, Surrey TW20 0EX, UK. [6]Department of Geophysics and Energy, Instituto Dom Luiz, Faculty of Sciences (IDL-FCUL), University of Lisbon, Campo Grande Ed. C1, Piso 1, 1749-016 Lisboa, Portugal. [7]Center of Marine Sciences (CCMAR/FCT), Universidade do Algarve, Campus de Gambelas, 8005-139 Faro, Portugal. [8]Andalusia Institute of Marine Sciences, Spanish National Research Council (ICMAN-CSIC), Republica Saharaui 2, Puerto Real E11519, Spain. [9]Spanish Institute of Oceanography, A Coruña Oceanographic Center, Paseo Marítimo A. Francisco Vázquez 10, A Coruña E15001, Spain.
*Corresponding author. Email: rleal@ieo.es

of geomorphologic and hydrodynamic factors in orchestrating a complex two-way flow pattern with major climatic implications.

## RESULTS

### MOW internal structure: A roller-coaster ride

West of 7.0°W, the MOW floods into the GoC basin at intermediate depths (Figs. 1, A and B, and 2). The flow drifts beneath ENACW propelled by barotropic subinertial and tidal forcing (*21*). Near the ocean bottom, velocity vectors exhibit a high degree of reproducibility, indicating bathymetric steering (Fig. 1C). Mean MOW velocity profiles also indicate vertical shear, with maximum velocities occurring above the seabed (Fig. 2A). This generates a well-mixed, turbulent benthic boundary layer at the base of the water mass and creates a discernible salinity signal linking MOW's pathway and bottom salinity. Salinity and velocity observations consistently show that the MOW pathway parallels the seafloor topography over the first 225 km west of Spartel (Fig. 2B). The initial 40-km descent from the Strait is followed by a 50-km clockwise turn before the flow divides horizontally into downslope, upper-slope, and midslope branches (Fig. 1C). We carried out a detailed inspection of the flow at 18 sections across the MOW (T1 to T18 from east to west; Fig. 1D). This examination reveals several smaller-scale arteries that diverge, meander, and/or coalesce because of the influence of submarine channels (Fig. 1D).

The bottom salinity gradient near the 36.3 isohaline shows the MOW to have a sharp edge over the slope, and a much poorly defined border along the shelf break (Fig. 1C). As the descending flow broadens (Fig. 2C) and salinity decreases (Fig. 2B), volume transport increases

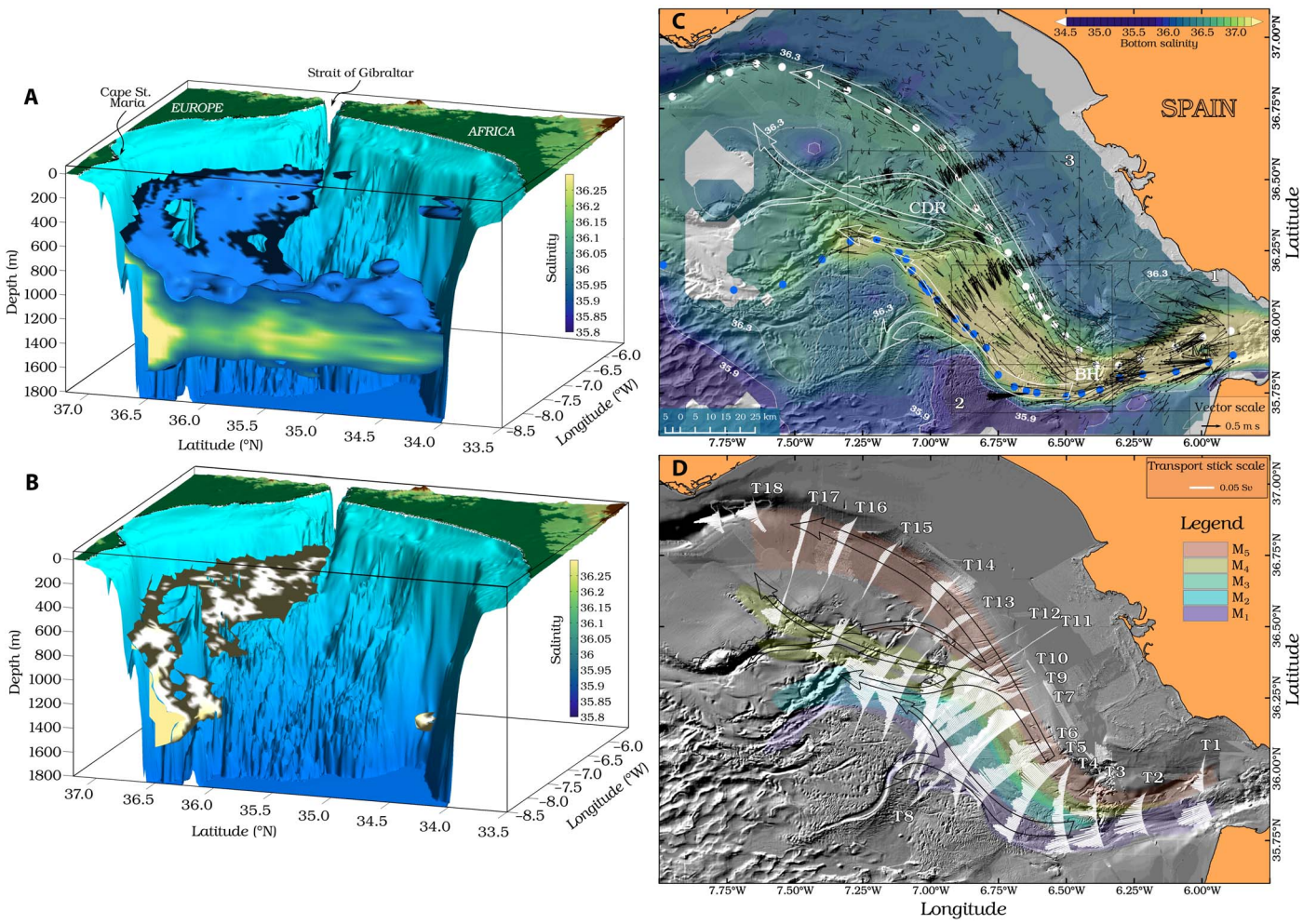


**Fig. 1. MOW in the eastern GoC.** (**A**) A three-dimensional (3D) view of the 35.90 isohaline as a buoyant, salty plume abutting the slope. (**B**) As in (A) but for the 36.30 isohaline and the along-slope undercurrent. (**C**) Shaded relief map of the GoC seafloor bathymetry with near-bottom instantaneous velocity vectors (black arrows) over salinity (color shades). The 35.9 and 36.3 salinity contours are included for visual reference. Colored dots indicate the approximate pathways of the historical upper and lower cores (see Fig. 2). White open arrows depict branching of the historical cores. Numbered squares indicate inset areas for the following figures. CDR and BH stand for the Cadiz Diapiric Ridge and Basement High, respectively. (**D**) Vertically integrated mean MOW volume transport vectors across a number of sections (T1 to T18, from east to west; all transects quoted throughout the text refer to this numbering). Colored bands outline the density-sorted MOW branches as described in the text. Black open arrows depict branching of the historical cores. The MOW plume expands as it stretches westward (A). West of 7.0°W, it separates from the seafloor to travel at mid-depths (800 to 1400 m). Bathymetric features influence salinities, velocities, and integrated transport (C), highlighting the role of the small-scale channels on transverse dispersion of saline water. Note that whereas discrete, near-bottom velocity observations appear to vary smoothly across the overflow (C), the vertically integrated transport within the MOW layer at (D) suggests individual branches that are forged upstream (D).

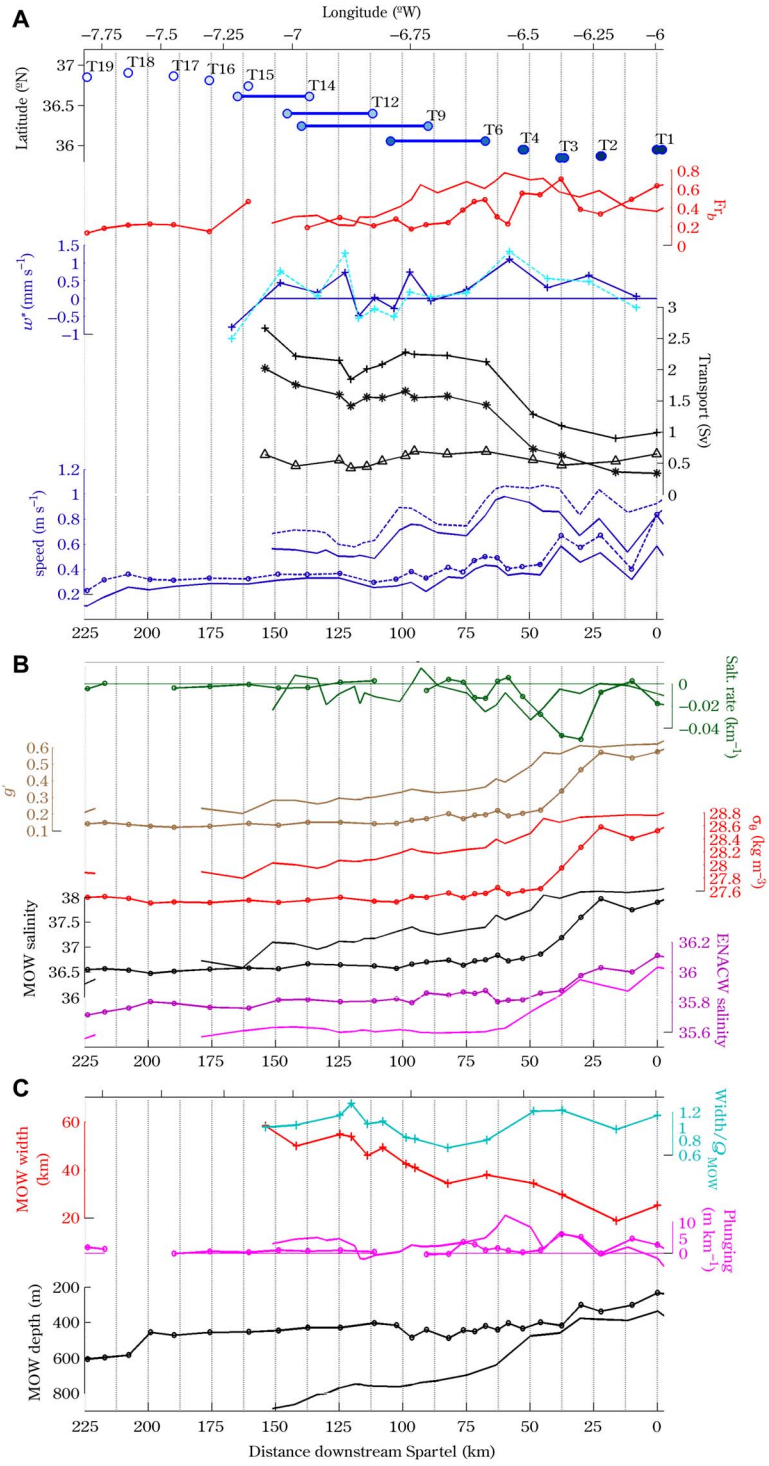


**Fig. 2. Upper and lower MOW evolution downstream of Spartel.** Representation of dynamical, hydrological, and geometrical properties versus distance (lower axis) and longitude (upper axis). (**A**) Dynamical properties. From top to bottom: Reference location of the upper and lower MOW boundaries at each section in Fig. 1D; bulk Froude number ($Fr_b$); entrainment velocity ($w^*$) calculated from salt (dashed line) and volume flux (solid line) conservation from T1 to T14; outflow ($Q_{MOW}$, crosses), pure MOW ($Q_{med}$, triangles), and entrainment ($Q_{ent}$, stars) transport across each section (the entrainment transport was estimated by subtracting $Q_{med}$ series from the integrated outflow transport $Q_{MOW}$; see fig. S8 for details); and MOW speed near the bottom (solid) and at the velocity maximum (dashed). (**B**) Hydrological properties. From top to bottom: Salinity loss rate, reduced gravity [$g'$, the acceleration of gravity ($g$) experienced by a parcel of density $\rho_1$ immersed in an ambient fluid of density $\rho_0$; $g' = g(\rho_1 - \rho_0)/\rho_0$], potential density anomaly ($\sigma_\theta$), MOW salinity, and ENACW salinity. Except for the latter (calculated at the ENACW salinity minimum), all curves show values near the seafloor. (**C**) Geometrical properties. From top to bottom: Normalized MOW width/$Q_{MOW}$ ratio across T1 to T14 (MOW width was taken as the distance between the inner and outer 36.3 isohalines near the bottom), MOW width, plunge rate, and MOW depth. Properties were either collocated at the (upper and lower) pathways outlined in Fig. 1C or averaged across the sections indicated in Fig. 1D. In all panels, lines marked with dots indicate values following the upper MOW (the lower MOW for lines without markers). Lines marked with crosses indicate values at each section in Fig. 1D. Note that this data set does not show the LC past T14.

from 1 to 2.7 Sv (Fig. 2A) by ENACW entrainment at discrete spots along the pathway (*22*). The highest entrainment velocities coincide with prominent bathymetric features between T2 to T4 and T11 to T14 (Fig. 2A and fig. S8). There is, however, substantial transport loss associated with downslope streams between T8 and T11 (Fig. 2A and fig. S2). ENACW salinities increase eastward from 35.6–35.8 to 36–36.1 (Fig. 2B).

Cross-stream heterogeneity intensifies as the MOW spreads. Most of the excess salinity (and, by extension, density) in the upper MOW becomes diluted within the first 50 km of its egress (Fig. 2B). The maximum salinity loss (0.05 $km^{-1}$) occurs west of 6.25°W, in the lee of the BH (Fig. 1C). At this point, flow accelerates (from 0.3 to 0.6 m $s^{-1}$) as it enters small channels (Figs. 1C and 2) (*23*, *24*) and proceeds down the upper slope. The lower MOW travels along a curved pathway around the southern BH flank (Fig. 1C). The prolonged descent and channel narrowing boost mean current velocities (up to 1.1 m $s^{-1}$) and bulk Froude numbers between T2 and T6 indicate points of intensified mixing (Fig. 2, A and B). Salinity decreases at a lower rate (0.02 $km^{-1}$) but over a longer distance (35 to 110 km downstream of Spartel). The salinity (and hence density) loss does not overcome the excess density that keeps the current flowing along the base of the water column, as illustrated by the downstream evolution of the reduced gravity $g'$ (Fig. 2B).

## Farewell to the Mediterranean basin: Exit and flow across the GoC

Current splintering at Spartel begins over a steep submarine ridge [Majuan Ridge (MR)], which splits the Gibraltar Channel into two subchannels (Figs. 1C and 3A). Near the bottom, high-salinity (>38) MOW meets water at the cap of the ridge with a salinity minimum (36.6). The outflow broadens downstream, whereas high-salinity waters wash over the northern shelf and extend southward along the channel. Instantaneous velocity observations (Fig. 3A) confirm a well-defined flow of 1 m $s^{-1}$ through the southern Spartel Channel. The northern channel supports a current (0.5 m $s^{-1}$) that is subjected to frequent flow reversals from tides, which can periodically outpace the mean outflow.

The time-averaged cross-strait structure (Fig. 3, B to D) shows Atlantic waters occupying the upper 150 m of the water column and forming a baroclinic jet over the MR with surface velocities greater than 0.5 m $s^{-1}$. The Strait also hosts a deeper, weaker, more barotropic branch transporting less saline ENACW to the south ($AI_1$ and $AI_2$; Fig. 3, B to D). The MOW resides at the base of the water column and is distinguished from shallower components by a sloping salinity and density interface (between 27 and 28.5 kg $m^{-3}$) that concentrates most subtidal variability (Fig. 3, B and C) (*4*). Eddy fluxes (positive correlations of tidal currents and tidally induced vertical displacements of the interface) around Spartel are much weaker than those observed elsewhere in the Strait, making the sill the westernmost hydraulic control point for the outflow (*25*). MOW dynamics are approximately semigeostrophic (*26*), with local acceleration, pressure gradient, and frictional terms balanced in the along-strait direction and geostrophic balance in the across-stream direction (in geostrophic motions, pressure gradient and Coriolis accelerations close the momentum balance). Here, the cross-strait 27.5 kg $m^{-3}$ isopycnal slope (mean interface) satisfies the expected geostrophic tilt (100 m over 26 km) taking layer-averaged MOW (−0.31 m $s^{-1}$, 36.30, 16.37°C) and AI (0.22 m $s^{-1}$, 37.30, 14.07°C) values. The ridge dividing the undercurrents creates two forks that experience different degrees of forcing. The slope in the density interface indicates a supergeostrophic northern branch and a subgeostrophic southern branch whose core banks against the African continental slope. Intense along-channel velocity and the relatively tight curvature of this branch (Fig. 3A) suggest both ageostrophic conditions and the necessary conditions for opposing secondary circulation accompanying the outflow [ageostrophy refers to motions where other terms (spatial accelerations, friction, or centrifugal terms) cannot be disregarded].

The mean flow exchanges at Spartel amounts to $Q_{ENACW}$ = 1.04 ± 0.11 Sv and $Q_{MOW}$ = −1.00 ± 0.10 Sv. Of these, −0.27 ± 0.03 (27%) flows into the Atlantic through the northern channel, whereas −0.73 ± 0.05 flows through the southern channel. The mean net flux into the Mediterranean is 0.05 ± 0.07 Sv. These values are similar to recent estimates [−0.85 ± 0.03 Sv; (*4*)] and promote convergence in the ongoing evaluation of the range of values reported in the literature (between −0.67 and −1.15 Sv).

## A complicated descent and asymmetric curving

Past Spartel, velocity vectors and isohalines converge as both MOW branches accelerate, superpose, and channelize over the 30-km southward descent from the Strait (between T1 and T3; see Fig. 3A and fig. S4). Transport reaches −0.90 ± 0.06 Sv across T2. The outflow arrives at BH at 6.40°W, which divides the bottom current into several branches distinguished by their haline properties that were developed upstream (labeled $M_1$ to $M_5$, from the deepest to the shallowest branch; Figs. 4A and 5A). A 6-km-wide and 550-m-deep passage guides the flow across T3 (0.72 of 1.10 ± 0.08 Sv across T3; $M_1$ in Fig. 4A). This feature is fed primarily by the southern Spartel Channel flow but may include a contribution from the northern Spartel Channel at its upper layer (fig. S5B). The current core banks against the southern flank of the pass at about 100 m above the channel thalweg (the axis of lowest elevation within a channel). Between the BH and the continental slope, the gentler northern Spartel Channel MOW (0.15 Sv) flows northwestward at 0.5 m $s^{-1}$ through a 430-m-deep trough ($M_5$). The two MOW flows mix and meet the BH ridge where decreased channel volume causes increased flow rates. The $M_4$ MOW component passes through a 3-km-wide, 530-m-deep gorge that zonally bisects the BH at 35.80°N (0.25 Sv). The remaining $M_2$ and $M_3$ components course around the BH. Scour depressions to the south of the BH have incisions of up to and over 120 m over a distance of 2 km (southern), whereas depressions to the north of the BH are around 300 m deep over a distance of 4.6 km (central) (Fig. 3A and fig. S5A).

Beyond the BH, bathymetric features induce mechanical separation, radial forcing, horizontal velocity divergence, and broadening of the MOW by a factor of 2 (Fig. 2C). MOW broadening comes at the expense of meridional density sorting into its individual components (Fig. 4C). The upper MOW component experiences sharp decelerations of bottom velocities (from −0.7 to −0.4 m $s^{-1}$; Fig. 2A) between T3 and T5 as a result of enhanced bottom roughness. Bathymetric features thus steer dissipation, entrainment stress, and mixing (*24*) as associated transport increases from 1.10 ± 0.08 Sv across T3 to 1.29 ± 0.05 Sv across T4 and ultimately reaching values of 2.13 ± 0.02 Sv across T5.

The MOW undercurrent is often depicted as creeping gently along a clockwise pathway that follows isobaths (*5*). Our velocity observations combined with detailed seafloor mapping across T4 (Fig. 4) reveal a more complex reality that includes several branches that travel with velocity, salinity, and density values that increase with depth. The branch that skirts the northern BH ($M_5$ in Fig. 4A) proceeds northwestward at 0.3 m $s^{-1}$ with salinities between 36.4 and 36.8 and $\sigma_\Theta > 27.0$ kg $m^{-3}$ (0.24 Sv). A southern channel hosts a faster (>1.2 m $s^{-1}$) and saltier

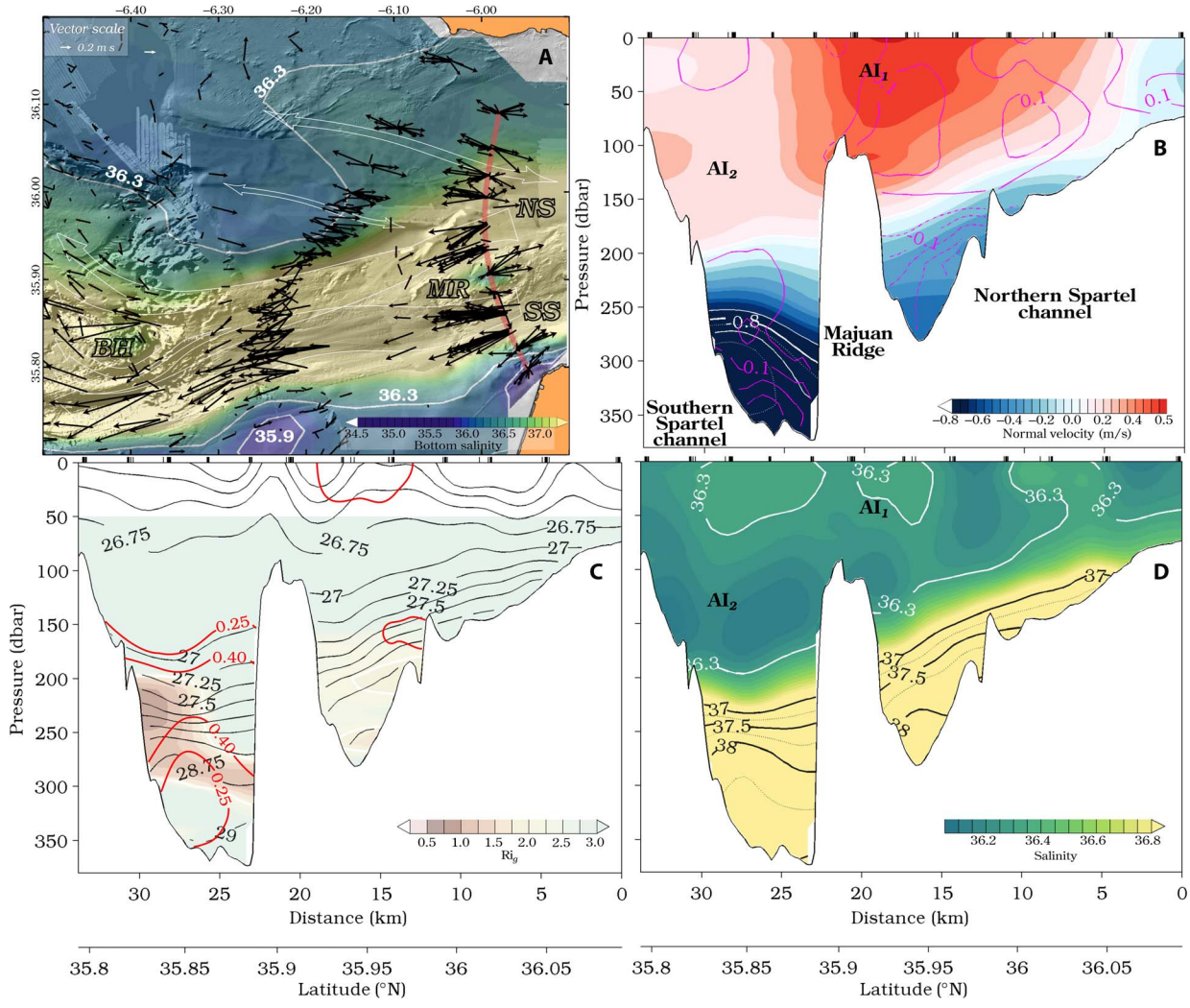


**Fig. 3. Leaving the Strait.** (**A**) Inset 1 from Fig. 1C. Small-scale bathymetric features guide the MOW as it passes Spartel (indicated with white open arrows). These include the MR, a straight, sloping channel, and a relatively rough BH dissected by two deep zonal gorges. The MR causes an initial division into coherent, separate flows across the northern (NS) and southern (SS) Spartel channels. Instantaneous velocity observations indicate less temporal variability for the southern flow than for the northern one, which experiences tidally forced current reversals. Past the ridge, both components appear to coalesce with the northern flow overriding the southern flow (fig. S4). The BH diverts as much as 70% of the transport through a southern channel. A maximum bottom velocity for the entire data set (1.82 m $s^{-1}$) was observed here (35.77°N/6.38°W) during the 201306I3S cruise (table S1). (**B**) Mean velocities (m $s^{-1}$; negative for westward flow) across T1 [red line in (A)]. The color scale is saturated beyond −0.8 m $s^{-1}$, and additional velocity contours (white lines) are included every 0.1 m $s^{-1}$. Magenta contours indicate tangential velocity every 0.05 m $s^{-1}$ (solid for southward and dashed for northward). Ticks at the top axis indicate the location of individual observations. The ridge separates two MOW forks residing at different depths. The more energetic, southern flow banks against the southern channel slope. (**C**) Gradient Richardson number ($Ri_g$) across T1. $Ri_g$ provides insight into the magnitude and vertical location of Kelvin-Helmholtz (K-H) instabilities. Despite the high density gradient and high static stability, the lowest $Ri_g$ values occur around the MOW-ENACW interface. Black contours indicate potential density anomaly ($\sigma_\theta$) every 0.25 kg $m^{-3}$. Red contours indicate the SD of velocities in (B) (m $s^{-1}$). After removal of tidal currents, variability remains relatively low everywhere except at the southern channel density interface, where high variability likely reflects seasonal forcing (*6*). (**D**) Mean salinity across T1. The color scale is saturated beyond 36.8, and additional contours are included every 0.25. Below the surface layer, the 36.3 isohaline approximately defines the interface between ENACW (with salinities down to 36.0) and MOW > 38.25.

(>37.75) ($M_1$ in Fig. 4A) branch transporting 0.44 Sv of the densest MOW ($\sigma_\Theta$ > 27.5 kg $m^{-3}$). Its core, coupled to a southern drift, flows zonally at about 50 m above the channel bed. A bottom-trapped and fast-moving flow with salinities greater than 37 sweeps radially across the central sector. This current couples with lighter ($\sigma_\Theta$ = 27 to 27.5 kg $m^{-3}$) overriding MOW and escapes through local BH gateways ($M_2$ to $M_4$ in Fig. 4B and fig. S5) to achieve a total transport of 0.61 Sv.

Bathymetric branching influences the slope of the MOW-ENACW interface. Onshore elevation is consistent with a gentle geostrophic $M_5$ flow skirting the slopes of the northern continental shelf. To the south, $M_1$ to $M_4$ are held between 35.75°N and 35.90°N by an inverted (in the geostrophic sense) interface (note the shape of the 27.5 kg $m^{-3}$ isopycnal in Fig. 4C). This indicates that bathymetric curvature disrupts the geostrophic balance of the current.

## Consolidation of the main branches

Past the BH, $M_1$ to $M_5$ evolve as parallel arteries guided by upper (500 to 620 m) and lower (660 to 750 m) erosive channels (UCh and LCh, respectively; Fig. 1D and fig. S1) within the middle slope. The ratio of the MOW width to its transport (width/$Q_{MOW}$) falls between T5 and

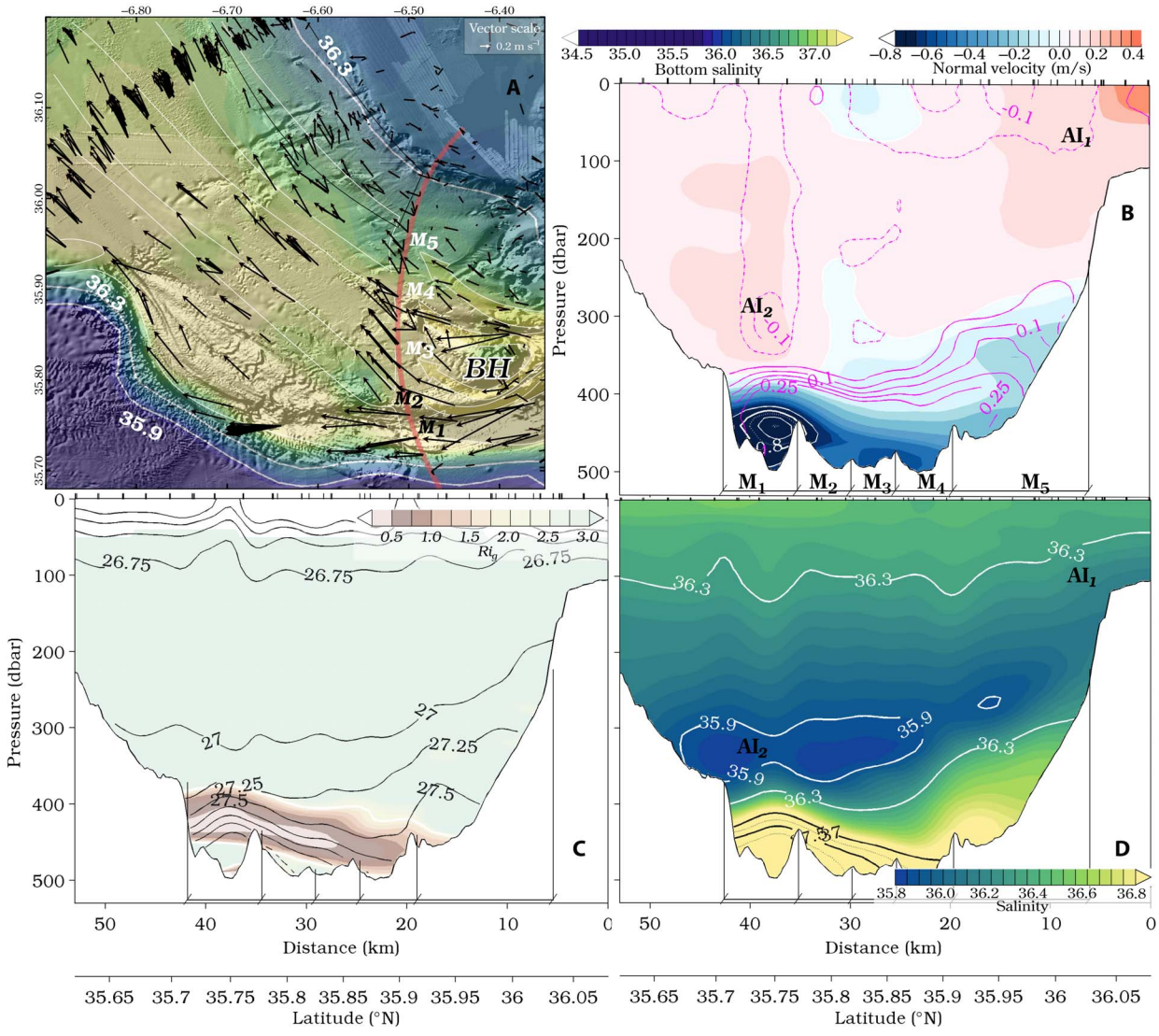


**Fig. 4. Asymmetric curving.** (**A**) Inset 2 of Fig. 1C. Individual MOW branches are labeled $M_1$ to $M_5$. Beyond the BH, the shallower $M_3$ to $M_5$ flows occupy curved (clockwise) channels, whereas the deeper $M_1$ and $M_2$ flows continue westward, and the overall MOW width expands by a factor of 2. Further downstream, $M_1$ traces a gentle clockwise arc, whereas $M_2$ courses northwestward along a nearly straight path. Both currents meet at 35.90°N/6.80°W. (**B**) As in Fig. 3B but for T4 [red line in (A)]. The MOW extends below two AI jets. It features diverging cores travelling along the slope at the base of the water column. Maximum velocities are constrained by the channel morphology at the southern border. (**C**) As in Fig. 3C but for T4. Strong vertical shears at the top of the MOW over $M_1$ to $M_3$ (and also at T3; fig. S5) exceed stratification (as measured by $N^2$) and bring $Ri_g$ close to the K-H instability limit. Increased likelihood of K-H instabilities, and hence vertical mixing, is higher east of 6.75°W (as shown in terms of $Fr_b$ in fig. S7). (**D**) As in Fig. 3D but for T4. Across-stream salinity structure below the 36.3 surface reveals the multicored MOW structure.

T8, suggesting that the diverse MOW components are brought together by the channels (Fig. 2C). These guide the 2.25 ± 0.08–Sv flow across T7 (Fig. 5B). The swifter (>0.6 m $s^{-1}$) $M_1$ with a salinity of >37.4 flows at 0.72 Sv along the LCh, whereas $M_4$ with a salinity of >37 flows at 0.63 Sv along the UCh. The core of $M_4$ (0.3 m $s^{-1}$) resides 40 m above the channel bed. Between these channels at 600 to 660 m, a 0.55-Sv flow from $M_2$ and $M_3$ (with a salinity of >37) travels along two narrow hanging troughs. This current consists of a 0.29-Sv $M_2$ flowing at velocities greater than 0.4 m $s^{-1}$ and a 0.26-Sv $M_3$ with velocities generally lower than 0.2 m $s^{-1}$. $M_5$ travels along the upper slope between 250 and 500 m as a 0.2–m $s^{-1}$ flow carrying 0.21 Sv with a salinity of <36.6. The southern flank of the upper slope between 6.80°W and 7.10°W includes a set of transverse furrows that carry small-scale and high-velocity overflows (for example, $Fs_3$ in Fig. 5A, with a bottom speed of >0.6 m $s^{-1}$). Each accounts for about 0.15 Sv of the total flow and may contribute to the downstream transport decrease from T7 to T11 (Fig. 1D and fig. S3). Given the abrupt decrease in depth (for example, in Fig. 1C), these saline conduits may influence basin-scale dynamics.

## MOW diversion in the central sector

As it flows north in the central GoC, the MOW encounters obstacles associated with the CDR, an offshore promontory at 35.30°N. These determine preferential pathways that eventually split the settling MOW at two different depth levels in what are historically referred to as the upper and lower Mediterranean cores (UC and LC, respectively; Fig. 5A) (*5*, *22*, *27*). Much of the MOW flow below 400 m (Figs. 1C and 5A and fig. S6) must either traverse intervening valleys or turn sharply to the left. The latter implies a shoreward force on $M_4$ and $M_5$ (contrary

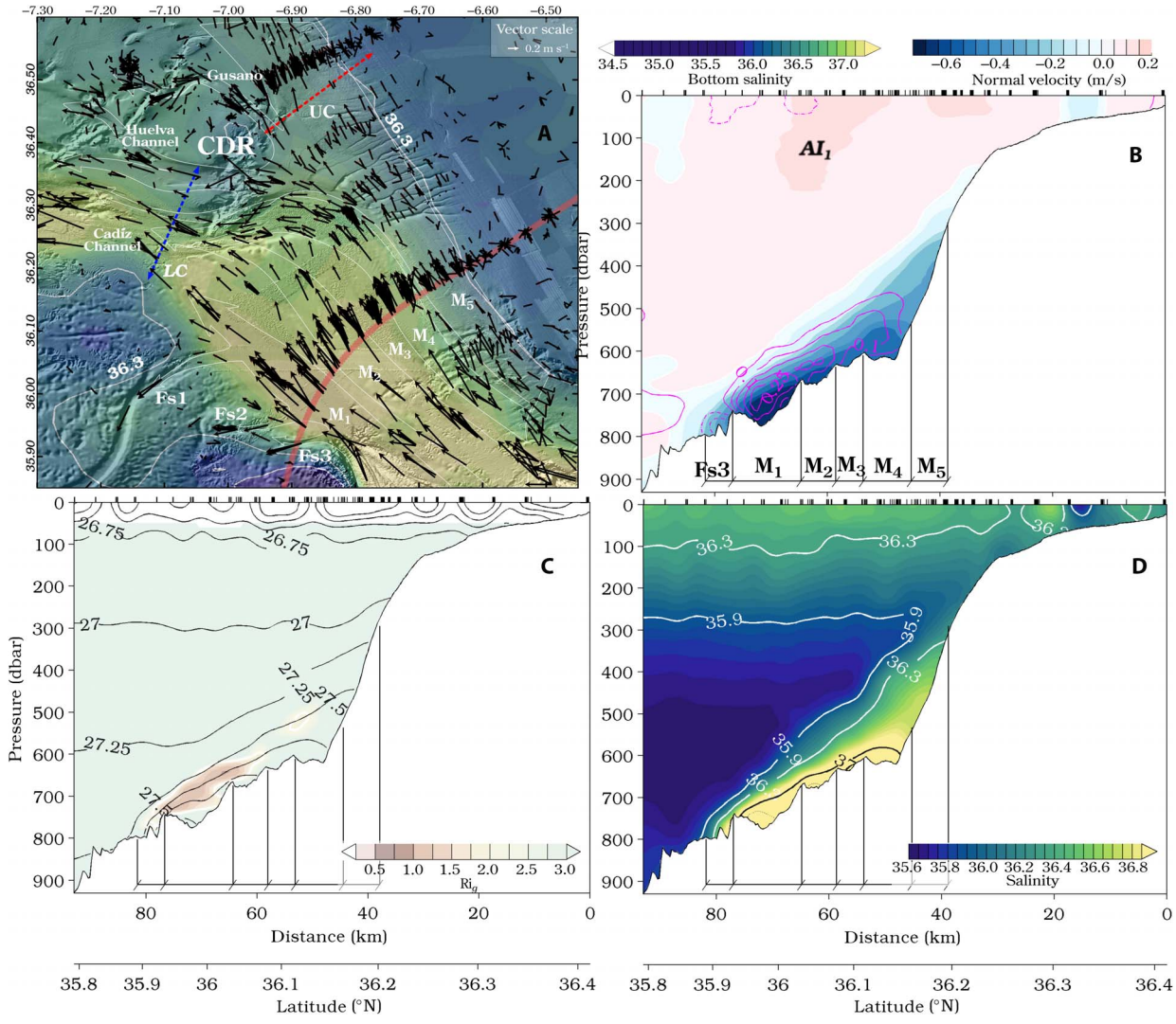


**Fig. 5. Consolidated MOW branches.** (**A**). Inset 3 of Fig. 1C. The CDR and the Gusano, Cadiz, and Huelva channels are labeled. Fs1 to Fs3 indicate the transverse furrows. The UC and LC are also outlined with dashed arrows. (**B**) As in Fig. 3B but for T7 [red line in (A)]. Individual MOW branches identified in (A) occupy every slope channel and the transverse furrow Fs3. (**C**) As in Fig. 3C but for T7. (**D**) As in Fig. 3D but for T7.

to the direction expected from bottom Ekman veering) and ascent of isopycnals [300 m over 30 km; fig. S5C; in excess of the expected geostrophic adjustment of 0.4 m $s^{-1}$ for a straight flow; (*28*)]. As in other submarine channels subject to rotation (*29*), this leftward bending leads to the formation of a coherent UC between the ridges and the shelf break (Fig. 5A and fig. S6). Across T13 (Fig. 1D), currents move at 0.3 m $s^{-1}$, transporting 0.60 Sv of the lightest MOW ($\sigma_\Theta$ = 27.2 to 27.4 kg $m^{-3}$ isopycnal). Downstream, smaller-scale channels, such as the Gusano, transport a significant component of the flow (0.12 Sv in this case; Fig. 5A). Likewise, the upper $M_4$ (about 0.30 Sv with a salinity of <36.9) flowing at 0.4 m $s^{-1}$ can overshoot the southern CDR at depths of 450 to 550 m and pass zonally through the Huelva Channel (fig. S6A). At this point, bottom velocities double after the current descends to 600 m before it splinters again past 7.10°W. By contrast, the lower $M_4$ follows a sharp zigzag pathway as it hits the ridge. At 36.25°N to 7.05°W, it encounters the deeper, northwestward-flowing $M_1$ to $M_3$. Both proceed through the Cadiz Channel to feed into the 1.7-Sv LC (about two-thirds of the MOW across T13; fig. S6) as a multicored undercurrent.

## DISCUSSION AND CONCLUSIONS

Traditional conceptions of MOW egress are based on relatively sparse current-meter observations (*8*, *30*), with the exception of the Baringer and Price's (*22*) absolute velocity data set [based on the integration of expendable current profiler (XCP) observed velocity shear and a rather arbitrary reference]. The exhaustive data set described here shows initial MOW circulation in unprecedented detail. It demonstrates precisely how the bathymetry and hydrodynamics of the Strait of Gibraltar convert a single-stream, dense overflow into a multicored, saline plume.

Just beyond the gateway, the MOW divides into several depth-sorted (and density-sorted) arteries flowing over and along curved bathymetric features (Fig. 1D). Its modification reflects spatiotemporal (*24*) entrainment and detrainment regimes (*30*) present along a complex pathway (*31*). Our observations indicate that spreading is topographically restricted, whereas mixing is favored by the topography, as the likelihood of K-H instability grows where the overflow accelerates in response to topography constraints. Past Spartel, the upper MOW undergoes rapid dilution (Fig. 2B) allowing for complex entrainment dynamics (during

entrainment, the MOW dilutes as it incorporates ambient fluid). The extreme density of the lower MOW allows it to travel as an unmixed arcing downflow that may experience detrainment and saline leakage contributing to mid-depth plume formation (during detrainment, a gravity current releases water to the ambient fluid). Both help explain transport loss between T1–T2 and T7–T12 (Fig. 1D) and increasing salinity of the overlying ENACW (*30*) that, in turn, contributes to plume dilution by entrainment of relatively warm, saline ENACW (*11*). All of these factors provide an alternate route for minor injections of salt whose impact on Atlantic salinities remains unclear.

Previous studies have described the outflow in terms of friction and centrifugal forces, which spread MOW through the depth sorting of density cores along an arcing channel (*32*). Entrainment and mixing of lighter components indicate an upper, geostrophic MOW, whereas Ekman veering within a frictional layer would pinch out a denser, deeper flow (*22*). Our observations reveal that the MOW undergoes an initial division as the overflow travels through the Strait, before entering the right turn (*33*). The rough, curving bathymetry modulates cross-stream heterogeneity, intensifies centrifugal terms {the ratio of centrifugal to Coriolis accelerations [curvature Rossby number; (*25*)] $R_c = \frac{U\beta}{fL} > 0.75$, where $f$ is the Coriolis parameter and β is the change of direction (74° or 1.3 radians) over a distance $L$ (19 km) for a MOW between −0.9 and −1.0 m $s^{-1}$} and constrains bottom Ekman dynamics, preventing simple and earlier MOW spreading from the Strait.

The exact history of the curving and bifurcated geomorphology of the Gibraltar Channel remains obscure but nevertheless holds consequences for ocean dynamics over the last ~5 million years. Pliocene outflow, which was probably weaker than presently observed flow rates (*9*), eroded into featureless and unconsolidated sediment to create the curved channels. A denser and more intense MOW during cold periods [late Pliocene and Quaternary; (*34*)] would have increased both channel relief and flow confinement (*35*). Prominent evidence of overflow and incision into channel flanks suggests, however, that the current lower MOW has outgrown these earlier templates (*36*).

Numerical models often use bulk parametrizations and low-resolution bathymetry to describe the MOW and its role in Atlantic climatic dynamics (*10*, *19*, *37*). In addition to temporal variability of Mediterranean and Atlantic water masses (*38*, *39*), the detailed description presented here reveals the complexities of the flow and its bathymetric interactions. The latter determines bottom current pathways, whereas the former can modify the seafloor through erosional and depositional processes. This feedback behavior likely operates in other interbasinal channels as well.

Observations such as those presented here provide high-resolution descriptions of overflows and can thus help to fine-tune and increase the predictive power of climate models. These can, in turn, be used to assess MOW production volume under different climatic scenarios and effects on local erosive power, salt flux, and other Atlantic oceanographic parameters. The flow description presented here also carries implications for NADW production and AMOC stability (*40*), both of which modulate Atlantic climate, as shown by the sedimentary record over the last 5.3 Ma (*6*).

## MATERIALS AND METHODS

### Bathymetric data

The Digital Terrain Model (DTM) combined data sets collected at different resolutions, assembled at 100-m spatial resolution using the Generic Mapping Tool (GMT, version 5.1.1) (*41*), as in the study of Becker (*42*). Data specifically included were the EuroMargins SWIM data set (*43*), bathymetric observations taken during the LIFE+ INDEMARES-CHICA project (*44*), the MAGRAMA Ecocartographical study (*45*), and the CONTOURIBER swath bathymetry data (*10*). The data set also incorporated multibeam sonar swaths collected during routine Instituto Español de Oceanografía (IEO) cruises aboard the R/V *Ramón Margalef* (EM710), R/V *Ángeles Alvariño* (EM710), and B/O *Miguel Oliver* (EM300). Data compilation included additional bathymetric metadata and DTM data derived from the EMODnet Bathymetry portal (*46*). We used the improved DTM as a reference boundary for CTD quality control (QC) and colocation of CTD and lowered acoustic Doppler current profiler (LADCP) observations. The DTM also served as an interpretational framework for hydrographic observations.

### CTD and LADCP data

The study involved analysis of hydrographic observations taken during IEO cruises dating back to 1997, previously collected data provided by several principal investigators, and compiled profile data distributed through SeaDataNet data resources (*47*), the National Oceanic and Atmospheric Administration (NOAA) Data Center (*48*), the International Council for the Exploration of the Sea (ICES) Marine Data Center (*49*), the British Oceanographic Data Centre (BODC) (*50*), the Coriolis Data Centre (*51*), the Systèmes d'Informations Scientifiques pour la MER (SISMER) (*52*), and PANGAEA (see table S1 for data sources) (*53*). Data were subjected to automated and manual QC procedures to remove duplicates and biased or spurious data following standard SeaDataNet protocols (*54*). Salinity is expressed in terms of the Practical Salinity Scale 1978 (PSS-78). Most of the LADCP profile database consisted of 2009–2017 IEO cruise data. These were processed using the inversion method and constrained by bottom-tracked and vessel-mounted ADCP (VMADCP) velocities where available (*55*). In these cases, VMADCP data were processed using the Common Ocean Data Access System (*56*). We also included SEMANE (Sortie des Eaux Méditerranéennes en Atlantique Nord-Est) [funded by Service Hydrographique et océanographique de la Marine, Direction Générale de l'Armement, Institut Français pour l'Explotation de la Mer, and Université de Bretagne Occidentale; (*57*)] data. The resulting database included 12,087 CTD and 4339 LADCP profiles.

To analyze near-bottom MOW spreading, we averaged CTD (LADCP) observations taken 15 m (40 m) or closer to the bottom or at depths representing 85% of the total depth range for profiles of areas shallower than 100 m. Both near-bottom and water column profile data were interpolated on a 0.025° × 0.025° × 25 m grid using Data-Interpolating Variational Analysis (DIVA) (*58*). In this analysis, the gridded fields are obtained as solutions to a cost function that optimizes the interpolation residuals on a finite-element grid adapted to the domain bathymetry. The main advantage of this method compared to other optimal interpolation routines is that it takes coastlines and other topographic/bathymetric features into account. DIVA analyses rely on specifying a correlation length scale ($L$) and a signal-to-noise ratio (SNR) (λ). The correlation length measures spatial significance of the data and was estimated ($L$ = 0.11°) by fitting the data correlation function to a theoretical function (*58*). The SNR represents confidence in the data and is derived from estimated measurement noise and significance error. We determined λ by cross-validation, removing random sets of observations and minimizing the root mean square of the residuals (λ = 8.4). To account for additional spatial smoothing, we used $L$ = 0.15° and λ = 8.0.

Temporal averages of property fields were produced on 500 m × 10 m vertical grids along several transects approximately perpendicular to both the bathymetric slope and the main direction of MOW

propagation (labeled T1 to T18 in Fig. 1D). The transect layout was set by the approximately quarterly STOCA time-series monitoring program. We applied a Gaussian smoothing filter to those grids with a horizontal scale of 5 km and a vertical scale of 20 m for hydrographic data (10 km and 30 m for velocity data). We generated an initial estimate of temporal variability by calculating the SD of all observations taken throughout each standard section (see Fig. 3C for example). The surface layer generally gave the largest temperature deviations due to seasonal heating cycles. Salinity and potential temperature showed little variability around both the ENACW salinity minimum and the MOW core. The largest deviations occurred around the density interface. This variability was up to two orders of magnitude larger for the Strait sections (that is, T1 to T3 in Fig. 1D) because of the stronger tidal influence (*25*, *59*). To improve the representativeness of mean velocity fields across these sections, we removed baroclinic currents from the four most energetic tidal components ($M_2$, $S_2$, $K_1$, and $O_1$) using tidal harmonics from a 3D, fully nonlinear, nonhydrostatic numerical model (*59*).

### Computation of MOW transports

Our CTD-LADCP and bathymetric data set allows calculation of an observation-based estimate of mean flows with a precise definition of the integrated area (that is, a well-constrained volume accurately representing the sea bottom and interface surfaces) that accounts for the asymmetric cross-strait flow. For each section in Fig. 1D, we calculated the MOW volume transport ($Q_{MOW}$) as the integral of the normal velocity over the area occupied by the flow according to

$$Q_{MOW} = \int_{z=-h(y)}^{z=-D(y)} \int_{y=y_{on}}^{y=y_{off}} u(y,z)\,dydz$$

for $u(y, z) < 0$, where $-D$ and $-h$ are across-shore variation bottom and interface depths, respectively, $u(y,z)$ is the velocity normal to the section, $y_{on}$ and $y_{off}$ are the cross-stream boundaries approximated by the 36.3 isohaline along the seafloor, and $dy$ and $dz$ are the cross-stream and vertical distance increments, respectively.

The calculation of flows across the Strait of Gibraltar from instantaneous measurements is not trivial. It requires the choice of a suitable interface to define both horizontal components. Sammartino *et al.* (*4*) discussed the use of the isohaline that maximizes the outflow (36.66 in that case), the isoline of maximum vertical shear, and the depth of maximum salinity gradient. In the present case, we use temporal averages, which we assume to represent steady-state conditions, wherein inflow and outflow are separated by the mean zero along-strait velocity surface. ENACW volume transport across Spartel was therefore calculated as

$$Q_{ENACW} = \int_{z=-h(y)}^{z=0} \int_{y=y_{on}}^{y=y_{off}} u(y,z)\,dydz$$

for $u(y, z) > 0$.

### Calculation of entrainment velocity

Besides the downstream evolution of properties near the seabed at both edges of the outflow (see Fig. 2), we used the averaged data to estimate the evolution of entrainment along the MOW pathway. We followed Baringer and Price's (*22*) approach in estimating the evolution of volume and salt flux. For the first case, we used the integrated continuity equation

$$\frac{\partial}{\partial \zeta}\left(\int_{z=-D(y)}^{z=-h(y)} \int_{y=y_{off}}^{y=y_{on}} u(y,z)\,dydz\right) = \int_{y=y_{off}}^{y=y_{on}} w^*\,dy$$

with $\zeta$ being the along-stream coordinate (positive downstream) and $w^*$ the entrainment velocity (positive downward). Downstream divergence (convergence) of the integrated transport between sections must be balanced by entrainment (detrainment). Likewise, for the salt flux

$$\frac{\partial}{\partial \zeta}\left(\int_{z=-D(y)}^{z=-h(y)} \int_{y=y_{off}}^{y=y_{on}} u(y,z)S\,dydz\right) = \int_{y=y_{off}}^{y=y_{on}} w^*\,S_{ent}dy$$

where $S$ is MOW salinity and $S_{ent}$ is the salinity of the entrained ENACW. Note that unlike Baringer and Price (*22*), who assumed a constant $S_{ent}$ = 35.6, we specifically included a spatially variable $S_{ent}$ (see fig. S8 for details).

### Calculation of gradient Richardson and bulk Froude numbers

We computed the gradient Richardson number as a measure of whether the flow has sufficient kinetic energy to induce mixing through breaking K-H instabilities (*22*). This is the ratio of stratification to the vertical shear

$$\mathrm{Ri}_g = \frac{N^2}{\left(\frac{\partial u}{\partial z}\right)^2 + \left(\frac{\partial v}{\partial z}\right)^2}$$

where $u(z)$ and $v(z)$ are the zonal and meridional velocity components and $N^2$ (the buoyancy frequency squared) is calculated as the vertical gradient of potential density referenced to the local pressure as (*60*)

$$N^2 = \frac{-g}{\rho_\theta}\frac{\partial \rho_\theta}{\partial z}$$

Theoretically, for a sheared, stratified flow, K-H instability emerges if $\mathrm{Ri}_g < 0.25$ (*22*). Note that $\mathrm{Ri}_g$ was computed from the mean, gridded vertical fields. Hence, these will render a smoothed, averaged $\mathrm{Ri}_g$ image. For comparison among cross sections, these are presented in Figs. 3 to 5 and figs. S2 to S6.

For an idealized two-layer flow, it is common to use the bulk Froude number ($\mathrm{Fr}_b$) as a layer approximation of the square-root inverse $\mathrm{Ri}_g$ (*22*)

$$\mathrm{Fr}_b = \left(\frac{\rho_o \Delta U^2}{gH\Delta\rho}\right)^{1/2}$$

where $\Delta U$ is the velocity difference and $\Delta\rho$ is the density difference between MOW and ENACW layers. The term $H$ represents the MOW layer thickness. Figure S7 shows the map illustrating the spatial representation of the outflow stability in terms of $\mathrm{Fr}_b$. Figure 2A and figs. S7 and S8 show its downstream evolution. Note that $\mathrm{Fr}_b$ was computed from the mean, gridded horizontal fields and will also render a smoothed, average picture.

## SUPPLEMENTARY MATERIALS

Supplementary material for this article is available at http://advances.sciencemag.org/cgi/content/full/3/11/eaao0609/DC1

fig. S1. Spatial distribution of CTD and LADCP observations used in this study on superimposed shaded relief of the study area.
fig. S2. Temporal and spatial distribution of CTD and LADCP observations.
fig. S3. Volume transport across a number of sections crossing the MOW pathway.
fig. S4. The southern Gibraltar Channel.
fig. S5. The Basement High.
fig. S6. The Cadiz Diapiric Ridge.
fig. S7. Spatial distribution of the bulk Froude number ($Fr_b$) computed from the gridded, mean fields over a swath bathymetric shaded relief map.
fig. S8. Evolution of the early MOW downstream of Spartel.
table S1. Sources for the hydrographic and velocity data used in this study.

## REFERENCES AND NOTES


1. S. Duggen, K. Hoernle, P. van den Bogaard, L. Rüpke, J. P. Morgan, Deep roots of the Messinian salinity crisis. *Nature* **422**, 602–606 (2003).
2. D. García-Castellanos, F. Estrada, I. Jiménez-Munt, C. Gorini, M. Fernández, J. Vergés, R. de Vicente, Catastrophic flood of the Mediterranean after the Messinian salinity crisis. *Nature* **462**, 778–781 (2009).
3. N. Loget, J. Van Den Driessche, On the origin of the Strait of Gibraltar. *Sediment. Geol.* **188-189**, 341–356 (2006).
4. S. Sammartino, J. García-Lafuente, C. Naranjo, J. C. Sánchez-Garrido, R. Sánchez-Leal, A. Sánchez-Román, Ten years of marine current measurements in Espartel Sill, Strait of Gibraltar. *J. Geophys. Res. Oceans* **120**, 6309–6328 (2015).
5. J. F. Price, M. O. Baringer, R. G. Lueck, G. C. Johnson, I. Ambar, G. Parrilla, A. Cantos, M. A. Kennelly, T. B. Sanford, Mediterranean outflow mixing and dynamics. *Science* **259**, 1277–1282 (1993).
6. F. J. Hernández-Molina, D. A. V. Stow, C. A. Alvarez-Zarikian, G. Acton, A. Bahr, B. Balestra, E. Ducassou, R. Flood, J.-A. Flores, S. Furota, P. Grunert, D. Hodell, F. Jimenez-Espejo, J. K. Kim, L. Krissek, J. Kuroda, B. Li, E. Llave, J. Lofi, L. Lourens, M. Miller, F. Nanayama, N. Nishida, C. Richter, C. Roque, H. Pereira, M. F. S. Goñi, F. J. Sierro, A. D. Singh, C. Sloss, Y. Takashimizu, A. Tzanova, A. Voelker, T. Williams, C. Xuan, Onset of Mediterranean outflow into the North Atlantic. *Science* **344**, 1244–1250 (2014).
7. P. L. Blanc, The opening of the Plio-Quaternary Gibraltar Strait: Assessing the size of a cataclysm. *Geodinamica Acta* **15**, 303–317 (2002).
8. M. García, F. J. Hernández-Molina, E. Llave, D. A. V. Stow, R. León, M. C. Fernández-Puga, V. Diaz del Río, L. Somoza, Contourite erosive features caused by the Mediterranean Outflow Water in the Gulf of Cadiz: Quaternary tectonic and oceanographic implications. *Mar. Geol.* **257**, 24–40 (2009).
9. M. Rogerson, E. J. Rohling, G. R. Bigg, J. Ramirez, Paleoceanography of the Atlantic-Mediterranean exchange: Overview and first quantitative assessment of climatic forcing. *Rev. Geophys.* **50**, RG2003 (2012).
10. F. J. Hernández-Molina, E. Llave, B. Preu, G. Ercilla, A. Fontan, M. Bruno, N. Serra, J. J. Gomiz, R. E. Brackenridge, F. J. Sierro, D. A. V. Stow, M. García, C. Juan, N. Sandoval, A. Arnaiz, Contourite processes associated with the Mediterranean Outflow Water after its exit from Strait of Gibraltar: Global and conceptual implications. *Geology* **42**, 227–230 (2014).
11. M. J. Bellanco, R. F. Sánchez-Leal, Spatial distribution and intra-annual variability of water masses on the Eastern Gulf of Cadiz seabed. *Cont. Shelf Res.* **128**, 26–35 (2016).
12. J. Ochoa, N. A. Bray, Water mass exchange in the Gulf of Cadiz. *Deep Sea Res. Part A Oceanogr.Res. Pap.* **38**, S465–S503 (1991).
13. M. A. Spall, P. L. Richardson, J. Price, Advection and eddy mixing in the Mediterranean salt tongue. *J. Mar. Res.* **51**, 797–818 (1993).
14. A. J. Williams III, Salt fingers observed in the Mediterranean outflow. *Science* **185**, 941–943 (1974).
15. L. D. Talley, *Physical Oceanography. Encyclopedia of Earth Sciences* (MacMillan Publishing, 1996), pp. 745–749.
16. K. P. Koltermann, V. V. Gouretski, K. Jancke, *Hydrographic Atlas of the World Ocean Circulation Experiment (WOCE). Volume 3: Atlantic Ocean*. M. Sparrow, P. Chapman, J. Gould, Eds. (International WOCE Project Office, 2011).
17. J. L. Reid, On the contribution of the Mediterranean Sea outflow to the Norwegian-Greenland Sea. *Deep Sea Res. Part A Oceanogr. Res. Pap.* **26**, 1199–1223 (1979).
18. Y. Jia, Formation of an Azores Current due to Mediterranean overflow in a modeling study of the North Atlantic. *J. Phys. Oceanogr.* **30**, 2342–2358 (2000).
19. A. Peliz, J. Dubert, P. Marchesiello, A. Teles-Machado, Surface circulation in the Gulf of Cadiz: Model and mean flow structure. *J. Geophys. Res.* **112**, C11015 (2007).
20. M. Gasser, J. L. Pelegrí, M. Emelianov, M. Bruno, E. Gràcia, M. Pastor, H. Peters, Á. Rodríguez-Santana, J. Salvador, R. F. Sánchez-Leal, Tracking the Mediterranean outflow in the Gulf of Cadiz. *Prog. Oceanogr.* **157**, 47–71 (2017).
21. M. L. Gründlingh, On the observation of a solitary event in the Mediterranean Outflow west of Gibraltar. *"Meteor" Forsch. Ergebn.* **23**, 3–46 (1981).
22. M. O. Baringer, J. F. Price, Mixing and spreading of the Mediterranean outflow. *J. Phys. Oceanogr.* **27**, 1654–1677 (1997).
23. M. Gasser, J. L. Pelegrí, J. D. Nash, H. Peters, J. García-Lafuente, Topographic control on the nascent Mediterranean outflow. *Geo-Mar. Lett.* **31**, 301–314 (2011).
24. J. D. Nash, H. Peters, S. M. Kelly, J. L. Pelegrí, M. Emelianov, M. Gasser, Turbulence and high-frequency variability in a deep gravity current outflow. *Geophys. Res. Lett.* **39**, L18611 (2012).
25. A. Sánchez-Román, G. Sannino, J. García-Lafuente, A. Carillo, F. Criado-Aldeanueva, Transport estimates at the western section of the Strait of Gibraltar: A combined experimental and numerical modeling study. *J. Geophys. Res.* **114**, C06002 (2009).
26. J. Candela, C. Winant, A. Ruiz, Tides in the Strait of Gibraltar. *J. Geophys. Res.* **95**, 7313–7335 (1990).
27. F. Madelain, Influence de la topographie du fond sur l'écoulement méditerranéen entre ledétroit de Gibraltar et le cap Saint-Vincent. *Cah. Océanogr.* **22**, 43–61 (1970).
28. R. Cossu, M. G. Wells, Coriolis forces influence the secondary circulation of gravity currents flowing in large-scale sinuous submarine channel systems. *Geophys. Res. Lett.* **37**, L17603 (2010).
29. D. R. Parsons, J. Peakall, A. E. Aksu, R. D. Flood, R. N. Hiscott, Ş. Beşiktepe, D. Mouland, Gravity-driven flows in a submarine channel bend: Direct field evidence of helical flow reversal. *Geology* **38**, 1063–1066 (2010).
30. C. Mauritzen, Y. Morel, J. Paillet, On the influence of Mediterranean water on the central waters of the North Atlantic Ocean. *Deep-Sea Res. I* **48**, 347–381 (2001).
31. P. G. Baines, Mixing in downslope flows in the ocean - plumes versus gravity currents. *Atmos. Ocean* **46**, 405–419 (2008).
32. P. C. Smith, A streamtube model for bottom boundary currents in the ocean. *Deep-Sea Res. Oceanogr. Abstr.* **22**, 853–873 (1975).
33. K. M. Borenäs, A. K. Wåhlin, I. Ambar, N. Serra, The Mediterranean outflow splitting—A comparison between theoretical models and CANIGO data. *Deep-Sea Res. Pt. II* **49**, 4195–4205 (2002).
34. A. Bahr, F. J. Jiménez-Espejo, N. Kolasinac, P. Grunert, F. J. Hernández-Molina, U. Röhl, A. H. L. Voelker, C. Escutia, D. A. V. Stow, D. Hodell, C. A. Alvarez-Zarikian, Deciphering bottom current velocity and paleoclimate signals from contourite deposits in the Gulf of Cádiz during the last 140 kyr: An inorganic geochemical approach. *Geochem. Geophys. Geosyst.* **15**, 3145–3160 (2014).
35. J. de Leeuw, J. T. Eggenhuisen, M. J. B. Cartigny, Morphodynamics of submarine channel inception revealed by new experimental approach. *Nat. Commun.* **7**, 10886 (2016).
36. A. Fildani, W. R. Normark, S. Kostic, G. Parker, Channel formation by flow stripping: Large-scale scour features along the Monterey East Channel and their relation to sediment waves. *Sedimentology* **53**, 1265–1287 (2006).
37. S. Legg, T. Ezer, L. Jackson, B. P. Briegleb, G. Danabasoglu, W. G. Large, W. Wu, Y. Chang, T. M. Özgökmen, H. Peters, X. Xu, E. P. Chassignet, A. L. Gordon, S. Griffies, R. Hallberg, J. Price, U. Riemenschneider, J. Yang, Improving oceanic overflow representation in climate models: The Gravity Current Entrainment Climate Process Team. *Bull. Am. Meteorol. Soc.* **90**, 657–670 (2009).
38. A. Bozec, M. S. Lozier, E. P. Chassignet, G. R. Halliwell, On the variability of the Mediterranean Outflow Water in the North Atlantic from 1948 to 2006. *J. Geophys. Res.* **116**, C09033 (2011).
39. J. García-Lafuente, C. Naranjo, R. Sánchez-Leal, S. Sammartino, M. J. Bellanco, J. C. Sánchez-Garrido, J. Soto-Navarro, On the origin of the seasonal and interannual T–S variability of the inflow through the Strait of Gibraltar. *Deep Sea Res. Pt. I* **101**, 38–53 (2015).
40. R. Ferrari, C. Wunsch, Ocean circulation kinetic energy: Reservoirs, sources, and sinks. *Annu. Rev. Fluid Mech.* **41**, 253–282 (2009).
41. P. Wessel, W. H. F. Smith, R. Scharroo, J. Luis, F. Wobbe, Generic Mapping Tools: Improved version released. *Eos. Trans. AGU* **94**, 409–410 (2013).
42. N. C. Becker, Painting by numbers: A GMT primer for merging swath-mapping sonar data of different types and resolutions. *Comput. Geosci.* **31**, 1075–1077 (2005).
43. N. Zitellini, E. Gràcia, L. Matias, P. Terrinha, M. A. Abreu, G. DeAlteriis, J. P. Henriet, J. J. Dañobeitia, D. G. Masson, T. Mulder, R. Ramella, L. Somoza, S. Diez, The quest for the Africa–Eurasia plate boundary west of the Strait of Gibraltar. *Earth Planet. Sci. Lett.* **280**, 13–50 (2009).
44. V. Díaz-del-Río-Español, G. Bruque-Carmona, L. M. Fernández-Salas, J. L. Rueda, E. González-García, N. López-González, D. Palomino, F. J. López-Rodríguez, C. Farias, R. F. Sánchez-Leal, J. T. Vázquez, C. Krutzky, A. Fernández-Zambrano, P. Marina-Ureña, V. Luque, T. Oporto, O. Sánchez-Guillamón, M. García, J. Urra, P. Bárcenas, M. P. Jiménez, R. Sagarminaga, J. M. Arcos, Volcanes de Fango del Golfo de Cádiz. Áreas de Estudio del proyecto LIFE+ INDEMARES (2014); www.repositorio.ieo.es/e-ieo/handle/10508/9584.
45. MAGRAMA, www.mapama.gob.es/es/costas/temas/proteccion-costa/ecocartografias/ecocartografia-cadiz.aspx.
46. EMODnet, www.emodnet-bathymetry.eu.
47. SeaDataNet data resources, www.seadatanet.org/Data-Access.

48. National Oceanographic Data Center, www.nodc.noaa.gov.
49. ICES Marine Data Centre, www.ices.dk/marine-data/Pages/default.aspx.
50. British Oceanographic Data Centre, www.bodc.ac.uk.
51. Coriolis Data Centre, www.coriolis.eu.org.
52. SISMER Systèmes d'Informations Scientifiques pour la MER, (www.ifremer.fr/sismer/index_UK.htm).
53. PANGAEA, (www.pangaea.de).
54. SDN, SeaDataNet QC procedures (2010), www.seadatanet.org/Standards-Software/Data-Quality-Control.
55. M. Visbeck, Deep velocity profiling using lowered acoustic doppler current profilers: Bottom track and inverse solutions. *J. Atmos. Oceanic Tech.* **19**, 794–807 (2002).
56. E. Firing, J. M. Hummon, Ship-mounted acoustic doppler current profilers, in *The GO-SHIP Repeat Hydrography Manual: A Collection of Expert Reports and Guidelines*, E. M. Hood, C. L. Sabine, B. M. Sloyan, Eds. (IOCCP R. No 14, ICPO 134, 2010); (www.go-ship.org/HydroMan.html).
57. X. Carton, L. Chérubin, J. Paillet, Y. Morel, A. Serpette, B. Le Cann, Meddy coupling with a deep cyclone in the Gulf of Cadiz. *J. Mar. Syst.* **32**, 13–42 (2002).
58. C. Troupin, A. Barth, D. Sirjacobs, M. Ouberdous, J.-M. Brankart, P. Brasseur, M. Rixen, A. Alvera-Azcárate, M. Belounis, A. Capet, F. Lenartz, M.-E. Toussaint, J.-M. Beckers, Generation of analysis and consistent error fields using the Data Interpolating Variational Analysis (DIVA). *Ocean Model.* **52–53**, 90–101 (2012).
59. J. C. Sánchez-Garrido, G. Sannino, L. Liberti, J. García-Lafuente, L. Pratt, Numerical modeling of three-dimensional stratified tidal flow over Camarinal Sill, Strait of Gibraltar. *J. Geophys. Res.* **116**, C12026 (2011).
60. T. J. McDougall, P. M. Barker, Comment on "Buoyancy frequency profiles and internal semidiurnal tide turning depths in the oceans" by B. King *et al. J. Geophys. Res.* **119**, 9026–9032 (2014).

**Acknowledgments:** We are indebted to the crews of the following research vessels (B/O) that supported data collection over the years of this study: *Cornide de Saavedra*, *Odón de Buen*, *Ramón Margalef*, *Ángeles Alvariño*, *Miguel Oliver*, and *García del Cid*. **Funding:** We also acknowledge funding and data provided by projects INGRES3 (CTM2010-21229), STOCA (IEO 2009), PESCADIZ (IEO), INDEMARES (LIFE07 NAT/E/000732+), MOC2 (CTM2008-06438-C02-01), MED-OUTFLOW (CTM2008-03422-E/MAR and CTM2010-11488-E), PELCOSAT (IEO), SEMANE (X. Carton), DILEMA (CTM2014-59244-C3-2-R), and INPULSE (CTM2016-75129-C3-1-R) as well as SISMER, PANGEA, IEO, ICES, BODC, and NOAA data centers. Additional funding was provided by the CONTOURIBER (CTM2008-06399-C04-01/MAR) project. Part of the research was conducted in the framework of the "Drifters" Research Group of the Royal Holloway, University of London, UK. **Author contributions:** R.F.S.-L. and J.L.P. conceived and designed the research. F.J.H.-M. and J.G.-L. refined the manuscript. R.F.S.-L. compiled, processed, and analyzed the data. R.F.S.-L. wrote the manuscript and prepared the figures. All authors read and commented on the manuscript. **Competing interests:** The authors declare that they have no competing interests. **Data and materials availability:** All data needed to evaluate the conclusions in the paper are present in the paper and/or the Supplementary Materials. Additional data related to this paper may be requested from the authors.

Submitted 9 June 2017
Accepted 24 October 2017
Published 15 November 2017
10.1126/sciadv.aao0609

**Citation:** R. F. Sánchez-Leal, M. J. Bellanco, L. M. Fernández-Salas, J. García-Lafuente, M. Gasser-Rubinat, C. González-Pola, F. J. Hernández-Molina, J. L. Pelegrí, A. Peliz, P. Relvas, D. Roque, M. Ruiz-Villarreal, S. Sammartino, J. C. Sánchez-Garrido, The Mediterranean Overflow in the Gulf of Cadiz: A rugged journey. *Sci. Adv.* **3**, eaao0609 (2017).

# The Mediterranean Overflow in the Gulf of Cadiz: A rugged journey

Ricardo F. Sánchez-Leal, María Jesús Bellanco, Luis Miguel Fernández-Salas, Jesús García-Lafuente, Marc Gasser-Rubinat, César González-Pola, Francisco J. Hernández-Molina, Josep L. Pelegrí, Alvaro Peliz, Paulo Relvas, David Roque, Manuel Ruiz-Villarreal, Simone Sammartino and José Carlos Sánchez-Garrido

*Sci Adv* **3** (11), eaao0609.
DOI: 10.1126/sciadv.aao0609